AIAA 2003-4583

Flow Visualization Measurement Techniques for High-Speed Transition Research in the Boeing/AFOSR Mach-6 Quiet Tunnel

Shin Matsumura and Steven P. Schneider
School of Aeronautics and Astronautics
Purdue University
West Lafayette, IN 47907-1282 USA

Scott A. Berry
NASA Langley Research Center
Hampton, VA 23681

39th AIAA/ASME/SAE/ASEE
Joint Propulsion Conference and Exhibit

20-23 July 2003
Huntsville, AL

Flow Visualization Measurement Techniques for High-Speed Transition Research in the Boeing/AFOSR Mach-6 Tunnel

Shin Matsumura* and Steven P. Schneider+
School of Aeronautics and Astronautics
Purdue University
West Lafayette, IN 47906 USA
and
Scott A. Berry∞
NASA Langley Research Center
Hampton, VA 23681 USA

ABSTRACT

Flow visualization experimental methods are developed for hypersonic boundary-layer instability and transition research. The techniques are applied to a scramjet forebody geometry in Purdue's Boeing/AFOSR Mach-6 Tunnel. Fluorescent oil-flow visualization techniques are used to complement the instability measurements obtained with temperature-sensitive-paints. Gross flow features such as separated flow regions can be detected and quantified. Temperature-sensitive-paint is used to measure the surface temperature distribution, and the boundary layer instability due to streamwise vortices is inferred from the computed heat-transfer rates. The mean heat-transfer rates are about a factor of ten larger than published 2-D laminar CFD data on the Hyper-X. Two major problems with the TSP technique applied in this facility are identified. The variation of the insulating layer thickness and the pressure sensitivity of the TSP introduce significant uncertainties. Despite these error sources, the small variations in the heat-transfer rate caused by the stationary instability, and its growth along the model are measurable.

INTRODUCTION

Hypersonic boundary-layer transition experiments performed in conventional hypersonic tunnels suffer from ambiguities due to high levels of freestream noise, mostly caused by the turbulent boundary layer along the nozzle wall [1]. At high Mach numbers, this turbulent boundary layer radiates noise in the form of eddy Mach wave acoustic radiation. This has a significant effect on the stability of the boundary layer growing on a model. Not only can it change the quantitative results, it can change the trends in boundary layer stability and transition altogether from that of flight [2-4]. For example, linear stability theory along with the e^N correlation for transition location predicts that transition onset is earlier on a 5º half angle cone than on a flat plate at Mach 3.5 [5]. Experiments done at NASA Langley under noisy conditions showed that transition occurred earlier on a flat plate, whereas under quiet conditions, linear stability theory was verified [5]. Many high-speed flight vehicle programs, such as the National Aerospace Plane [6 7], X-33 [8, 9], high-speed missiles [10, 11], the shuttle [12-15], etc., have been hindered by ambiguous transition results obtained in conventional facilities.

The Boeing/AFOSR Mach 6 Tunnel at Purdue University was designed and built for studying high-speed boundary layer transition under quiet conditions to obtain improved data regarding boundary layer stability and transition. Construction of the tunnel was finished during the spring of 2001, and tunnel shakedown has started [16]. Currently the tunnel runs quiet only at very low unit Reynolds numbers. Results from tunnel shakedown experiments are being used to make modifications to the tunnel to enable quiet flow to higher unit Reynolds numbers. These modifications include changing the boundary layer bleed slot geometry at the nozzle throat [17, 18], polishing the downstream sections of the nozzle, and removing the double-wedge centerbody from the diffuser [19]. In addition, the necessary instrumentation is being developed at the same time. This includes an automatic vertical traverse system for pitot-tubes and hot-wires [20], a glow-discharge perturber to introduce controlled disturbances into the flow [21], construction of a vibration isolated optical bench, the installation of a large Plexiglas window [22], and the development of temperature and pressure sensitive paint systems (TSP and PSP) for surface measurements [23, 24].

For the present research, the instability of stationary streamwise vortices was investigated on a scramjet forebody model. The streamwise vortices leave striation marks in the surface temperature

---

* Research Assistant, Student Member, AIAA.
+ Associate Professor, Associate Fellow, AIAA.
∞ Visiting Researcher, Aerothermodynamics Branch

distribution measured using TSP. The details of the experimental results and analysis are documented in Ref. [25]. TSP has been used extensively for transition detection and flow visualization in the past, but the aim of this research was to obtain measurements which can be used to infer growth of stationary disturbances that cause transition. This paper presents the details of the TSP measurement technique used for this research. The oil-flow visualization technique is also presented. Results from oil-flow experiments complemented the TSP measurements by revealing flow features such as the separation onset, which were very difficult to measure with TSP.

THE BOEING/AFOSR MACH-6 QUIET TUNNEL

The Boeing/AFOSR Mach-6 Tunnel is a Ludwieg-tube blow-down wind tunnel. A general schematic of the facility is shown in Figure 1. The air storage tank is a 122 ft. driver pipe that connects directly to the contraction without gates, valves, or screens. This helps to maintain a smooth flow into the contraction. Downstream of the driver pipe is the contraction and nozzle, with a boundary layer bleed at the throat to start a new boundary layer for the supersonic expansion. The nozzle is designed to maintain a laminar boundary layer as long as possible by reducing the Görtler instability with a gentle wall curvature, reducing the Tollmien-Schlicting instability through non-uniform heating, and eliminating cross-flow instability with an axisymmetric design [26]. In addition the majority of the nozzle is polished to a mirror finish to meet the roughness Reynolds number requirement of no more than about 10-12 to avoid roughness effects [27]. The second throat downstream of the test section is set with a double diamond wedge, which is also where the model sting is supported. More details of the mechanical design are reported in Refs. [16, 28-30]. Also included are test results of components, and measurements of the nozzle coordinates.

A double burst diaphragm separates the vacuum tank from the upstream sections of the tunnel. The entire tunnel, including the nozzle and test section, is pressurized to the desired initial total pressure. An expansion fan travels upstream into the driver pipe when the diaphragm bursts, which starts the tunnel. The total pressure drops quasi-statically about every 0.2 sec. as the expansion wave reflects back and forth inside the driver tube. The total run time is 7-8 seconds.

A tunnel configuration which provides quiet flow continues to be sought. Several modifications have been made to the throat and boundary layer bleed geometry. This results in slightly different flow conditions, and a single value cannot be placed on the flow conditions (such as the Mach number) to represent all of the tunnel shakedown experiments that have been performed. The freestream Mach number and noise level variation for the different throat geometries tested are shown in Figures 2 and 3. All of these measurements were made with a Kulite pressure transducer in pitot-mode on the tunnel centerline, 84.63±1/16 inches downstream of the nozzle throat. The reader is referred to Ref. [17] for the detailed descriptions of the eleven cases shown here. For all cases the Mach number is between 5.6 and 6. A single data point at a Mach number 4.8 is shown at a total pressure of about 8 psia, which is probably caused by separation in the nozzle. Currently, the noise levels are typical of conventional wind tunnels, of about 1-5 %.

The total temperature variation during the run is modeled using the isentropic relation in Equation 1.

$$\frac{T_0}{T_{0,i}} = \left[\frac{P_0}{P_{0,i}}\right]^{\frac{\gamma-1}{\gamma}} \tag{1}$$

Here, γ is the ratio of specific heats, and T_0 and P_0 are the total temperature and pressure respectively, with the subscript "i" denoting the initial value prior to tunnel startup. This relation has also been used for the Mach-4 tunnel [31]. Results using this theory have been compared to cold-wire measurements in the Mach-6 facility, and show that the measurements are always slightly higher [20]. The reason for this has not been resolved yet. Refs. [17, 20] also show the Mach number profiles in the test section. With the exception of the data at one atm., all the profiles show fairly good uniformity. All the experiments performed as part of this research were conducted at a total temperature of 160 °C and total pressure between 80-130 psia. Using a Mach number of 6 as a representative value, the unit Reynolds number ranges from about 1.7-2.7 million /ft.

TEST MODEL

The Hyper-2000 geometry was obtained from the Hyper-X program office, after consulting several organizations for a geometry that represents air-breathing hypersonic vehicles of current interest. The model consists of three compression surfaces and the chines. It is truncated at the combustor inlet. The compression surfaces have angles of 2.5, 8, and 11 deg. to the freestream with the model at zero angle of attack. These angles are identical to the Hyper-X geometry. A schematic of the compression ramp portion is shown in Figure 4, and a picture of the windward surface is

shown in Figure 5. The model is approximately a fifth-scale model of the actual flight vehicle, and is 11.78 in. long with a span of 5.619 in. at the trailing edge. The compression surfaces have a width of 2.85 in.

The leading edge has a nearly square cross-section, and not a smooth radius due to machining limitations. The thickness of the leading edge at several spanwise stations was measured by pressing the model into a lead sheet [32]. The resulting profiles left in the lead sheet were examined under an optical comparator. Measurements of the leading edge thickness were then taken along the span at several locations, and are shown in Figure 6. The thickness varies from about 8 to about 12.2 mils. The measurements are believed to be accurate to about 0.5 mils. These measurements results in a mean leading edge thickness of 10.8 mil., with an RMS value of one mil.

FLUORESCENT OIL-FLOW VISUALIZATION EXPERIMENTAL METHOD

Oil-flow experiments were performed to visualize overall flowfield features which cannot be readily measured with TSP. The separation line near the first compression corner is of primary interest for the Hyper-2000 geometry. Generally it is very difficult to measure the separation onset with TSP because the change in heat-transfer-rate in the separation zone is not significant enough to cause a noticeable temperature difference. Oil-flow experiments also give an understanding of the surface streamlines and any weak vortices which do not show up in TSP experiments.

Two slightly different approaches for conducting oil-flow tests were attempted. The first and most common technique utilizes small dots of oil to trace out the surface streamlines. The dots of oil are typically pigmented in such a way as to maximize contrast with the background model surface. Here, a fluorescent pink pigmentation (Dayglo Color Corp.) was used. Applying the dots to the surface can be a time-consuming process requiring some skill and patience to disperse just the right size, density, and distribution of dots. For the present study the dots were applied by quickly flicking the bristles of a small paintbrush heavy with oil. Here, a thin layer of clear oil was wiped onto the model prior to applying the dots. This base coat helped to allow the oil dots to move more easily during the tunnel run. The oil-dot technique can be considered a bit of an art when it comes to capturing and visualizing flow features that require significant time to develop, such as the oil-accumulation line that indicates separation.

The second technique, a painted-oil approach, requires significantly less skill and patience, as the pigmented oil is simply spread evenly over the model surface with a large paintbrush. Due to a much larger volume of pigmented oil on the surface, the accumulation lines representative of separation and the attenuation lines representative of vortex scrubbing develop much faster. The major drawback of this second approach is that the surface streamlines are harder to detect within the overall oil movement.

Dow Corning's silicone oil was used for these experiments. Three viscosity grades were available, 100, 200, and 350 cs. A 20 and 50 cs viscosity oil were also available, but were not used because of concerns that these viscosity oils could damage the Plexiglas window. The 200 cs viscosity oil resulted in the best images with the painted-oil approach, whereas the 100 cs oil resulted in the best images with the oil-dot technique. A sample image from this technique prior to a tunnel run is shown in Figure 7. The image shows a pre-run photograph of the oil-dot density in the compression corner region of the model, with the upstream portion of the model to the right. The approximate locations of the compression surfaces and corners are marked with white lines for clarity.

Digital video and high-resolution cameras were used to record the oil movement during the tunnel run. The model was illuminated with blue light. An orange or red filter was used on the cameras to capture only the fluorescence from the oil, and not the blue light reflections from the window and tunnel wall. An orange filter was consistently used with the digital camera because a red filter seemed to block too much of the fluorescence. The quality of the videos was identical regardless of the filter color, and consequently a newer and cleaner red filter was used.

Once the oil was applied to the model, the facility was closed up and prepared for a run by pressurizing to the desired settings. To minimize the time in which the oil could droop on the model, the tunnel settling time required for the driver air to reach equilibrium was reduced from the typical 10-30 minutes [19] to about a minute. The total time between oil application and tunnel run was on the order of 15 minutes. The video camera was started prior to starting the tunnel, and the higher resolution digital camera took four images spaced about 0.5 sec. apart, about 6 sec. into the tunnel run, immediately preceding tunnel unstart. The unstart process washed away most of the flow features which developed over the 7-8 sec. of Mach 6 flow. This development of the flow features over time from the video is illustrated in Figure 8. In Figure 8A immediately after tunnel startup, the oil has not moved enough to reveal the major flow features of interest yet.

Figure 8B is an image 6.5 sec. later. The separation line is clearly seen in this image, which is represented by the bright line immediately upstream of the first compression corner. The presence of streamwise vortices on the second and third compression ramp is also seen in this image. Figure 8C is an image taken 0.75 sec. later, which is estimated to be about 0.25 sec. after tunnel unstart. The oil accumulated at the separation line has been washed away, and the separation line is no longer clearly visible. Finally, Figure 8D shows an image taken after another 0.25 sec. In this image, the accumulated oil has been completely washed away, and all evidence of the separation line has been destroyed.

TEMPERATURE-SENSITIVE-PAINTS

A brief summary of the TSP technique will be given here. More extensive and complete descriptions are documented in Refs. [33-35]. TSP is used to measure the global temperature distribution of the model surface during the tunnel run. Arrays of thermocouples are traditionally used to measure surface temperature and heat flux distributions in wind tunnel experiments. Such techniques require large amounts of labor and have high installation costs. Also, the spatial resolution of these techniques is limited to the number of probes that can be installed in the model. TSP's are much simpler to apply on models, and are significantly less expensive. TSP has been used for various flow visualization and quantitative heat-transfer-rate measurements, such as forward and backward facing steps at supersonic conditions [36], a waverider geometry [37], cones and wing-body geometries in shock tunnels [38, 39], and boundary layer transition detection on wings and airfoils [40-42].

A general schematic of a TSP layer over a model surface is shown in Figure 9, which is adapted from Ref. [43]. The actual temperature-sensing layer is composed of luminescent molecules imbedded in a binder material, usually some sort of polymer-based coating. For metallic wind tunnel models with high thermal diffusivity and conductivity, an insulation layer is applied on the model surface first. This decreases the heat-transfer between the TSP layer and the model, resulting in a larger temperature change in the thin temperature-sensing layer. This in turn results in a higher signal-to-noise ratio, and allows the use of simplified heat-transfer models for data reduction.

TSP works under the thermal quenching principle, where the luminescent molecules absorb a particular wavelength of light that depends on the luminescent chemical used, and emits red-shifted light at an intensity that depends on the surface temperature. As the temperature increases, the thermal energy of the excited luminescent molecule also increases, and the emission intensity decreases. The luminescent material and binder are dissolved in solvents so that they can easily be applied to the model surface with a brush or spray gun. The polymer binder is an important ingredient of luminescent paint systems, since it serves to adhere the paint to the model surface, but also influences the pressure and temperature sensitivity, and the response time as well.

A CCD camera is most commonly used to capture the emitted light from the TSP. The temperature of the model surface can then be determined by applying a calibration that relates the model temperature to the emitted light intensity, using what is known as the intensity-based method. With this intensity-based method, which is used for this research, a reference image is taken at a known temperature (wind-off image). A second image is then taken during the tunnel run (wind-on image). The ratioing of these two images eliminates most of the effects from non-uniform lighting and painting. The model surface temperature can then be determined through a calibration curve, either performed prior to the wind tunnel testing on a TSP sample, or in-situ during the wind tunnel test. A general procedural schematic of this process is illustrated in Figure 10, which is taken from Ref. [44]. In-situ calibration results in more accurate measurements, but requires thermocouples strategically placed in the model [45]. The decay rate or phase-shift of the emission from a pulsed excitation source can also be measured, with the lifetime method. This alternative has offered some advantages with pressure-sensitive-paints and thermographic phosphors, and should be a possible means of improving the TSP measurement system as well [46-49].

TEMPERATURE-SENSITIVE-PAINT PROPERTIES AND CALIBRATION

Several luminophores, binder materials, and insulators have been discovered and developed over the years. A partial list and sample calibration data of some luminophores are listed in Refs. [33, 34]. In a past experiment in the Mach-4 facility, Ru(bpy), which is short for Tris(2,2'-bipyridyl) dichloro-Ruthenium(II) hexahydrate, has been used successfully [23]. For this research, Ru(phen), which is short for Dichlorotris(1,10-phenanthroline) ruthenium(II) hydrate, is used instead. This luminophore has been shown to be well suited for use in short-duration facilities [38, 45].

A comparison of the Ru(phen) calibration against Ru(bpy) showed the former to have a slightly higher

sensitivity above room temperature (Figure 11). The reference condition is taken at 297 deg. K here. Both of these calibrations were done at atmospheric pressure, with the same excitation light source and CCD camera used for the actual wind tunnel testing. The chosen binder for this research is DuPont's Chroma Clear polyurethane auto-paint. Again, this has been used successfully in the past [38, 45].

Many of the Ruthenium-based luminophores are also known to be sensitive to pressure, an undesirable characteristic for TSP's. Polyurethane binders help to reduce this because they have low oxygen permeability, but they do not eliminate the problem [50]. Figure 12 shows pressure calibrations of the current TSP for three separate hold temperatures of 25, 34, and 43 deg. C. The reference condition is taken at atmospheric pressure. There is a luminescence intensity change of nearly 6-8 % from atmospheric pressure down to tenths of a psia, but below about 0.4 psia, the variation with pressure is at most a percent, which is acceptable in terms of the resulting uncertainty.

The temperature calibration was repeated with the pressure held at 0.07 psia. This data is compared against the calibration performed at atmospheric pressure in Figure 13. Also shown are a few calibration data at 127 psia. The calibration at vacuum and atmospheric pressure is nearly identical up to about 320 deg. K, but then the sensitivity slightly decreases. This is probably related to the increased pressure sensitivity at the elevated temperatures, where oxygen quenching of the excited luminophores become significant compared to the effects of thermal quenching. The calibration at high pressure is also identical, at least in the available temperature range. These datasets imply that the temperature sensitivity is more or less independent of the pressure. However, this does not necessarily mean that the wind-off and wind-on images could be taken at two different pressures, as shown by the pressure calibration data shown in Figure 12. Pressure calibration data is not available above atmospheric pressure, but it is expected that the effect will be significantly larger if the calibration could be performed up to the 120-130 psia range.

The insulation layer affects the sensitivity and accuracy of the heat transfer model used in reducing the data to heat transfer rates. Mylar films such as those used for remote-controlled airplane applications are well suited [51]. However, these are not suitable for three-dimensional models, and an insulating layer must be painted onto the model, although this introduces the issue of non-uniform thickness distribution over the model surface, which can typically be about a factor of two or so. For the present research the same binder paint is used for the insulation layer as well. The thermal conductivity and diffusivity of this coating is quoted as 0.48 W/(m-K) and 2.7x10-7 m2/s respectively, between the temperature range of 293-323 deg. K [45].

Often times, a white pigment is added to the insulation layer to enhance the reflectivity of the temperature-sensing layer above the insulator. DuPont's Ti-Pure R-900 titanium dioxide (TiO_2) powder is used for this research. Two thermal properties are known for this particular material: a thermal conductivity of 8.8 W/m-K and a specific heat of 799 J/kg-K, as quoted by the manufacturer [52]. The addition of TiO_2 softens the insulator layer, which allows for easier polishing during model preparation. However, it increases the thermal conductivity. The insulation layer is only a few percent TiO_2 by weight, so this should not cause significant uncertainty problems.

TEMPERATURE-SENSITIVE-PAINT EXPERIMENTAL SETUP

A general schematic of the experimental setup is shown in Figure 14, and an image of the setup is shown in Figure 15. A 4 in. blue LED source (ISSI LM4 464 nm) containing 341 individual LED's is used as the excitation light source. A 12-bit CCD camera (Photometrics Sensys 0401E) is used to acquire the images. The Hyper-2000 model is visible through the window. A long-pass filter with a cut-off wavelength of 500 nm is used on the CCD camera lens to block any reflected blue light. The entire setup is placed inside a Lexan® safety enclosure, and then covered with black fabric to isolate the imaging system from the room lights. Turning off the room lights can easily eliminate most of the ambient light, but procedurally it was much more efficient to keep the room lights on constantly, and it also facilitated the operation of the tunnel.

The CCD camera must be activated manually in the present setup, and cannot be triggered by an external source. As a result, the image acquisition time with respect to tunnel startup can only be repeated to within 0.1-0.5 sec. A 5-volt DC signal is outputted from the camera while the shutter is open. This signal is fed into two oscilloscopes (LeCroy 9304/9314 AM). One of them records the signal from a Kulite pressure transducer mounted in the plenum section of the boundary layer bleed at the nozzle throat. The rapid decrease in pressure caused by the tunnel startup and the signal from the camera together can be used to record the image acquisition time relative to tunnel startup. The second oscilloscope records the signal from a Kulite pressure transducer mounted at the entrance to the contraction. This signal combined with

the camera signal is used to measure the total pressure during image exposure.

The wind-off image is taken at vacuum pressure since the static pressure along the model surface is only about 0.05-0.4 psia during a run, while the model is believed to be at an isothermal temperature. It was believed that this should reduce the uncertainty in applying the temperature calibration due to the pressure sensitivity of the TSP. The camera exposure time is adjusted during this process to fill the CCD bit-well. Typically the exposure time is between 50-200 ms, depending on the position of the LED source and camera, and the thickness of the TSP layer.

IMAGE PROCESSING

The wind-on and wind-off images will always have misalignment due to model motion relative to the camera, which is probably caused mostly by the recoiling of the tunnel at startup. For this facility, the curved window surface adds distortion to the images as well. In general the misalignment is caused by deflection of the model under aerodynamic load. Ref. [53] notes that this is usually the dominant error source in TSP experiments. This misalignment must be corrected using image registration techniques, and then resectioned to a grid, so that the image coordinates can be related to model coordinates.

Several forms of equations have been used in the past for image registration, such as the projective transform [54], the general power series [34, 55, 56], the general polynomial series [57], and Delaunay triangulation [58, 59]. Ref. [60] compares the accuracy of a few of these equations on a PSP image of a rigid model and deflective model. The wing model shows significant deflection compared to the sting mounted model, and is also more similar to the experiments done for this research. Here, a 3rd order polynomial and Delaunay triangulation give the best results.

The aligned images are then mapped onto the surface coordinates using resectioning methods. Various techniques are available here as well, such as the affine transformation [57], perspective and isometric projection [61], and the direct linear transformation (DLT) [56, 62], which is a reduced form of the collinearity equations of photogrammetry. More sophisticated methods that involve techniques used for computer vision are also being developed, and the theoretical foundations for such techniques are discussed in Ref. [63].

The two image processing steps were combined into a single step for this research. The wind-off and wind-on images, which showed at most a few pixels of misalignment, were directly mapped to a two-dimensional grid. The grid was constructed by isometrically projecting the coordinates of the registration marks to a plane perpendicular to the back surface of the model. This technique essentially eliminates the z-coordinate of the registration marks, or the depth of the marks in and out of the image. This allows the entire image processing to be done in two dimensions. The unknown coefficients can be solved for each image by constructing a system of linear equations relating the mark locations in the image to their grid coordinates. Better results were obtained by using more marks than the number of unknowns and solving the over-determined system in a least squares sense. The simulated annealing algorithm was used for the least squares fitting [64].

This image processing method was tested and validated on a set of sample images. In addition, a systematic attempt was made at understanding the optimal locations for the registration marks. The general rule of thumb is to spread out the marks throughout the image, and place them where the image movement is the largest. For this test a total of 56 marks were distributed evenly as possible, using a thin felt-tip permanent marker mounted in a milling machine with a coordinate readout display. The locations of the marks are shown in Figure 16.

The wind-on and wind-off images from a particular set of experiments showed an RMS misalignment of about a pixel. The misalignment against the grid was about 11 pixels. These misalignments are illustrated in Figure 17. The registration marks in the image and their corresponding grid locations are shown. The misalignment to the grid is significant, which results from the distorting effect of the window and from the fact that the camera is not oriented perfectly perpendicular to the image. The window acts as a cylindrical lens and stretches the image vertically.

An optimization routine was used to attempt to optimize the locations of the registration marks, for a particular type and order of an image registration equation, and a set number of points to use. This discrete variable optimization was performed using a genetic algorithm routine [65]. A standard penalty function was used to enforce the number of points to use. The objective function was the RMS misalignment of the marks to the grid computed using all 56 registration marks, after applying the constructed image registration equation. The fitness function is shown below in Equations 2 and 3.

$$I = P_{RMS} + z * MAX[\frac{Npts}{Ntotal} - 1,0] \quad \text{if } N_{pts} > N_{set} \quad (2)$$

$$I = P_{RMS} + z * MAX[\frac{Ntotal}{Npts} - 1,0] \quad \text{if } N_{pts} < N_{set} \quad (3)$$

Here, P_{RMS} is the RMS pixel misalignment, z is the penalty factor, N_{pts} is the number of points used to construct the image registration equation as determined from the optimization routine, N_{total} is the total number of registration marks, and N_{set} is the desired number of points to use to calibrate the equations. A penalty factor of 0.01 was effective, and was used for all cases. The optimization was stopped when the best fit did not improve over 5 generations.

The 1st and 2nd order polynomial, the 1st order power series, and the projective transform were tried. Higher order equations had too many degrees of freedom which introduced waviness, and actually resulted in a larger misalignment than the unprocessed images. The resulting RMS pixel misalignments are summarized in Figure 18. The figure shows that there are an optimal number of points to use. The 1st order polynomial and the power series result in the least performance because they cannot correct the curvature effects. The 2nd order polynomial gives the best results, and was adapted as the standard method for this research, shown below in Equation 4 and 5. Based on the data presented in Figure 18, it was also decided that using about 15 registration marks is good enough.

$$x = a_0 + a_1x' + a_2y' + a_3x'y' + a_4x'^2 + a_5y'^2 \quad (4)$$

$$y = b_0 + b_1x' + b_2y' + b_3x'y' + b_4x'^2 + b_5y'^2 \quad (5)$$

The genetically-optimized mark coordinates are shown in Figure 19, for the cases where 6, 12, and 17 marks were used with the 2nd order polynomial. The plot does not show any clear pattern as to which mark locations have the dominant effects. All three cases however do show a distribution of marks throughout the model surface, and are not all concentrated on a particular region of the model. This probably leads to the conclusion that the number of marks being used and the form of the image registration equation has the dominant effect, and that the location of the individual marks is of secondary importance, as long as the marks are distributed evenly along the model. The image shown in Figure 17 was corrected using the 2nd order polynomial, calibrated using 41 points. The resulting image is shown in Figure 20. The horizontal edges of the model are now more or less straight, unlike before where a curvature and a vertical drift could be seen. Also, the overall image has vertically shrunk, which is the result of correcting the vertical image-stretching effect from the cylindrical window.

HEAT-TRANSFER RATE DATA REDUCTION MODEL

The measured temperature distribution on the model is used to compute the heat-transfer rate. The unsteady heat transfer rate is assumed to be governed by the semi-infinite one-dimensional heat conduction equation. A diagram is shown in Figure 21, and the governing equation is shown in Equation 6.

$$\frac{\partial T}{\partial t} = \alpha \frac{\partial^2 T}{\partial y^2} \quad (6)$$

Here T is temperature, t is time, y is the distance from the surface, and α is the thermal diffusivity of the paint material.

Various forms of this equation have been used to compute the heat transfer rates [66]. For TSP experiments, two techniques seem to be especially popular, the discrete Fourier's Law [33, 36-38, 40, 51, 67] and the transient model for unsteady heat transfer rates [33, 39, 41]. The discrete Fourier's Law is used for this research, which is shown in Equation 7.

$$q = \frac{k}{L}(T - T_M) \quad (7)$$

Here, q is the heat transfer rate, k is the thermal conductivity, L is the insulator thickness, T is the temperature measured during the tunnel run, and T_M is the model substrate temperature. This steady-state model assumes that the model temperature and thermal conductivity stays constant, and the temperature-sensing layer is thin compared to the insulating layer. Ref. [37] compares the heat transfer rates computed with this model to a more sophisticated model that takes account effects such as the finite thickness of the insulator, and heating from the front and back surface, and shows that the results agree very well.

The modeling of the heat penetration process using the discrete Fourier's Law results in a temperature profile that is linear with depth into the insulator. The response time τ of the TSP is determined by how long it takes for this profile to reach steady state, which is proportional to L^2/α. For typical paintings the insulator and TSP layers are 3-5 and 0.5-1 mils thick respectively, which result in a response time of about 0.01-0.06 sec, using a thermal diffusivity of 2.7×10^{-6} m^2/s. The unsteady startup process of the tunnel usually takes about 0.25 sec., so ideally an image should be taken about 0.3 sec. after the diaphragms burst. However, this level of precision and repeatability requires electronic triggering of the CCD camera,

which will be developed and used for any future research with TSP's.

The thickness of the paint layer is measured using an eddy-current coating gauge (Elcometer Model 456). The spatial variation of the insulator thickness varies for each painting, and it is difficult to universally quantify this variation. The insulator thickness distribution for a particular painting is shown in Figure 22. The spatial coordinates of the measurement locations are accurate to only about an eighth of an inch. This data represents 495 measurements on the compression ramps. The thick and thinner spots in the painting are clearly illustrated. Also shown is a finer grid constructed by a two-dimensional interpolation and extrapolation of the measured data. More sophisticated schemes such as spline interpolations were tried, but these methods failed near the edges due to their nonlinearity.

Figures 23-25 shows the heat transfer rate distribution computed from the measured thickness distribution and the surface temperature. In Figure 23, the mean thickness (3.54 mils) is used throughout the image. The image is very smooth, clearly showing the overall trends. In Figure 24, the model is broken into four regions (three compression ramps and the chines) and a mean thickness value is used for each separate region (3.23, 4.28, 3.70, and 3.54 mils respectively). This should decrease the error due to the large variations in the insulator thickness, but results in a discontinuous heating distribution. In Figure 25, the interpolated thickness distribution is directly applied. The variation in the thickness causes significant variations in the computed heat-transfer rates.

A quantitative comparison of the heat transfer rates along the streamwise coordinate is shown in Figure 26. Each set of data is the spanwise average of 171 pixels. The data for the first two methods results in nearly an identical heating distribution on the first ramp. The sudden decrease seen with the second method at about 7 inches is caused by the discontinuous thickness. The third method contains several false peaks, and it is even arguable that the overall trends do not agree. Also, the leading edge heating is greater by about 50 %. The nature of the differences in the heating distributions makes it difficult to quantify a single uncertainty value for each method. However, it is clear that the first method results in the cleanest data for instability analysis. Using a single insulator thickness value is not desirable due to the large variations in the thickness, but was chosen as the preferred method, given the emphasis on boundary-layer instability in this research.

The mean heat-transfer rate distribution along the streamwise coordinate at two unit Reynolds numbers are compared to previously published CFD data [68] in Figure 27. The data only on the first compression ramp is shown, where the boundary-layer is most likely laminar. The data presented is a spanwise average at each streamwise location. The streamwise coordinate is normalized by the full vehicle length at the model scale, and the heat-transfer rates are normalized by the Fay and Riddell stagnation point heat-transfer rate [69] on a one-foot radius sphere scaled to the model size. The figure reveals two unexpected problems with the current data. The experimental heat-transfer rates are higher than the computations by an order of magnitude, and the data for the two unit Reynolds numbers show significant variations.

Three possible sources of these discrepancies have been identified and are listed below, along with possible approaches to resolve the problem.

1. The uncertainty in the computed heat-transfer rate is directly proportional to the insulator thickness variation. Use an adhesive tape which would provide a constant thickness for the insulator instead. However, applying tape to this model is not trivial, since the geometry is three-dimensional with surface curvature, corners, and breaks. Using multiple pieces of tape is also not an option, because any gaps or steps would generate undesired disturbances which will contaminate the instability measurements.
2. The temperature of the model increases significantly between tunnel startup and image acquisition. This is especially likely near the leading edge where the model is very thin. Apply insulating material to the leeward side to reduce the net heating to the model. Use a more sophisticated heat-transfer model where unsteady, multi-layer, and multi-dimensional [70] effects are modeled.
3. The measured temperature distribution during the run is significantly higher due to the pressure sensitivity of the TSP. The effect of pressure on the TSP luminescence is small between atmospheric and vacuum pressures, but the sensitivity from vacuum to high pressures is not known. If the response time to pressure is on the order of seconds (due to the slow oxygen diffusion in the binder), then it might be more accurate to take the wind-off image at high pressure rather than at vacuum.

Currently the third point above is suspected to be the dominant error source. This issue was investigated by comparing two TSP images taken at no-flow conditions, with pressures of 0.05 and 127 psia. The

model temperature was allowed to equilibrate for a few hours, and for both images the model temperature was 28.4 deg. C. The ratio of these two images is shown in Figure 28. Because the two images are taken at the same temperature, the intensity ratio should more or less be one, if there is no pressure effect. However, the figure shows that the image taken at 0.05 psia is about 30 % brighter than the image taken at 127 psia. This would result in significantly different surface temperature measurements and computed heat-transfer rates, depending on what pressure the wind-off image is taken at.

This effect is illustrated in Figure 29. Here, the normalized heat-transfer rate is shown near the first compression corner. As with Figure 27, the experimental data shown is an average over the span of the ramp portion. Depending on the pressure condition of the wind-off reference image, the heat-transfer rates are significantly different. The effect is large enough to change the sign of the heat-transfer rate. This data also implies that the response time of the TSP to pressure may need to be taken into account, since using a wind-off image at full stagnation pressure under-predicts the heating, and the use of a wind-off image at vacuum over-predicts the heating.

Despite these problems, instability analysis was carried out on the available data using a wind-off image at vacuum. The fluctuating component of the spanwise heat-transfer rate distributions are normalized by the mean heat-transfer rate. This should factor out most of the error, as long as the error in the mean heat-transfer rate is present in the magnitude of the fluctuations as well. The instabilities are quantified with a spectral analysis using Welch's averaged periodogram method, which is a routine available in Matlab. The power spectral densities (PSD) are then integrated in the wave-number range of relevance to obtain the power content. This information is then used to quantify the growth rate of the instability waves.

SAMPLE OIL-FLOW VISUALIZATION RESULTS

An oil-flow image with the painted-oil approach is shown in Figure 30, at a unit Reynolds number of 2.72 million/ft. The color scale has been converted to grayscale in order to enhance the contrast. The separation line immediately upstream of the first compression corner is evident from the bright line, which is caused by the accumulation of the oil. The separation line is brighter on the lower part of the model because of the tendency of the oil to flow down the vertically-oriented model in the time it takes to prepare for a tunnel run after painting the oil onto the model. Streamwise vortices on the second and third compression surfaces are also visible starting around 8 inches from the leading edge, which is 0.75 inches downstream of the first compression corner.

These images were useful for providing the separation line, and the parametric trend of the separation line was extracted from several images to quantify the behavior against unit Reynolds number, as shown in Figure 31. A second order polynomial is fitted to each set of data. The first compression corner is also shown for reference. A slight asymmetry is present for each case, which is probably caused by the combined effects of an asymmetric leading edge, a slight yaw in the model orientation, a non-uniform oil layer, the spatial uncertainty in the image-processing of about 0.05-0.07 inches, and error in extracting the data points from the images.

The reattachment line is better seen in the images taken with the oil-dot technique, shown in Figure 32 at the same unit Reynolds number. The separation zone is evident by the region at about 7 inches from the leading edge where the oil dots have not been washed away significantly. It is still difficult to quantify the reattachment line in this image, but it does reveal the approximate extent of the separation zone.

SAMPLE TEMPERATURE-SENSITIVE-PAINT EXPERIMENTAL RESULTS

A sample non-dimensional heat-transfer rate image from Ref. [17] is shown in Figure 33. The insulator thickness measurement was not available for this case. Consequently, the mean-heat transfer rate on the first compression ramp between 7.05-7.27 inches was used to normalize the data. This process factors out the insulator thickness and thermal conductivity if a constant value is assumed throughout the model. The total pressure, temperature, and unit Reynolds numbers were 118 psia, 760 deg. R., and 2.58 million/ft. Five roughness strips 4 mils thick are spaced 5/8 inches apart on the leading edge. Three of the vortices generated by them are visible ahead of the first compression corner. The outer two vortices get swept away onto the chine by the outward directed cross-flow. The breakdown of the vortices on the second compression ramp is clearly visible.

Figure 34 is an image with the 2.25 mil thick roughnesses spaced 0.16 inches apart. The total pressure and temperature was 127.2 psia and 779 deg. R respectively, giving a unit Reynolds number of 2.67 million/ft. The regularly spaced streaks structures imply the presence of streamwise vortices. The increased number of vortices generated by the increased number of roughness is evident compared to Figure 31.

The spanwise heat-transfer rate variations at three streamwise stations (marked with dashed lines in Figure 34) are shown in Figure 35. Each set of data is an average over a streamwise distance of 0.45 inches (61 pixel columns) to reduce noise. For this figure, the averaging window was doubled from what is normally used for quantitative analyses, so that the fluctuations are clearly visible. The growth and the decay of the fluctuations caused by the streamwise vortices are illustrated. The decrease in the peak-to-peak magnitude of the fluctuations from 8.97 to 10.09 inches suggests transition onset somewhere in between.

The PSD of the fluctuating component of the heat-transfer rate at 8.97±0.45 inches is shown in Figure 36. The figure shows a peak at 5.23 cycles/inch. The wavelength for this wave-number (number of cycles per unit length) is 0.19 inches, which corresponds well with the 0.16 inch roughness spacing taking into account the slight spanwise spreading. The PSD between 4.18 and 6.27 cycles/inch is integrated to obtain the streamwise power distribution. The power distribution is then normalized by the maximum power on the third ramp for each case, and is shown in Figure 37 for a range of unit Reynolds numbers. It is not clear what this amplitude ratio physically represents, but seems to give reasonable and clear trends. The growth occurs earlier and the peak on the second compression ramp increases with unit Reynolds number. This expected trend implies that the value of the peak amplitude ratio and streamwise location corresponding to it might be related to the transition onset. Comparison of these results to transition onset, obtained from hot-wire and/or reliable mean heat-transfer rate measurements, and stability computations is now necessary to relate these experimental results to the stability of the boundary-layer and transition.

CONCLUSION

Oil-flow visualization and temperature-sensitive-paints are used for high-speed boundary-layer transition research in Purdue's Boeing/AFOSR Mach-6 Tunnel. The techniques are currently applied to the Hyper-2000 scramjet forebody. The addition of fluorescent pigmentation to the oil and the use of a blue light source successfully eliminated reflections off the window. The oil-flow experiments mainly provide qualitative information about the overall flow structures, but quantitative measurements such as the separation onset are also attainable. Two oil-flow approaches were tried as part of this research. The traditional oil-dot technique shows the separation zone, but the 200 cs viscosity oil does not move enough during the limited tunnel run time to be able quantify the spatial extent of the separation zone. On the other hand, the painted-oil approach does not show the reattachment point, but the separation onset shows up very clearly.

Temperature-sensitive-paint is also used to measure the surface temperature distribution to infer the growth of streamwise vortices. The systematic trends seen with Reynolds number suggests that the growth of the fluctuating heat-transfer rates is related to boundary-layer instability and transition. However, several problems with the current implementation of the TSP technique to this facility have been identified through comparison of the results to CFD data. A constant thickness adhesive tape should probably be used for the insulator. The thickness variation with the painted approach results in significant uncertainty. This problem could not be corrected even if several thickness measurements are made and used in the form of a thickness grid.

The operating characteristics of Ludwieg tube-type facilities, of pressurizing the test section to full stagnation pressure, introduces difficulty in obtaining a reasonable wind-off reference image. The use of a wind-off image at high pressure under-predicts the heating, and a wind-off image at vacuum pressure over-predicts the heating. The sensitivity of the TSP to pressure thus has a significant impact on the qualitative results. The pressure sensitivity of the TSP and its response time to pressure change must be quantified and known to improve the quantitative measurements.

ACKNOWLEDGEMENTS

The authors would like to thank the research group headed by Prof. John P. Sullivan consisting of Jim Gregory, Chihyung Huang, and Hirotaka Sakaue at Purdue University for the use of their CCD camera. They also took part in a significant number of discussions regarding the development of the measurement technique. The members of the PSP/TSP group at the National Aerospace Laboratory of Japan headed by Dr. Keisuke Asai also provided valuable advice and expertise. Finally, the first author is supported by NASA Langley Grant NAG1-02047, and the third author is a visiting researcher from NASA Langley under the Floyd Thompson Fellowship program.

REFERENCES

[1] Schneider, S. P. and Haven, C. E. Quiet-Flow Ludwieg Tube for High-Speed Transition Research. *AIAA Journal*, 33(4):688-693, April 1995.

[2] Pate, S. R. Effects of Wind Tunnel Disturbances on Boundary-Layer Transition with Emphasis on Radiated Noise: A Review. Paper 80-0431, AIAA, March 1980.

[3] Pate, S. R. and Schueler, C. J. Radiated Aerodynamic Noise Effects on Boundary-Layer Transition in Supersonic and Hypersonic Wind Tunnels. *AIAA Journal*, 7(3):450-457, March 1969.

[4] Schneider, S. P. Effects of High-Speed Tunnel Noise on Laminar-Turbulent Transition. *Journal of Spacecraft and Rockets*, 38(3):323-333, May-June 2001.

[5] Chen, F.-J., Malik, M. R., and Beckwith, I. E. Boundary-Layer Transition on a Cone and Flat Plate at Mach 3.5. *AIAA Journal*, 27(6):687-693, June 1989.

[6] Defense Science Board, Report of the Defense Science Board Task Force on the National Aerospace Plane (NASP). AD-A201 124, September 1988.

[7] Defense Science Board, Report of the Defense Science Board Task Force on National Aero-Space Plane (NASP) Program. AD-A274 530, 94-00052, November 1992.

[8] Thompson, R.A., Hamilton II, H.H., Berry, S.A., Horvath, T.J., and Nowak, R.J. Hypersonic Boundary-Layer Transition for X-33 Phase II Vehicle. Paper 98-0867, AIAA, January 1998.

[9] Palmer, G., Kontinos, D., and Sherman, B. Surface Heating Effects on X-33 Vehicle: TPS Panel Bowing, Steps, and Gaps. Paper 98-0865, AIAA, January 1998.

[10] Hingst, U.G. Laminar/Turbulent Flow Transition Effects on High-Speed Missile Domes. AGARD CP-493, pg. 27.1-27.8, 1990.

[11] Korejwo CDR, H.A. and Holden, M.S. Ground Test Facility for Aerothermal and Aero-Optical Evaluations of Hypersonic Interceptors. Paper 92-1074, AIAA, February 1992.

[12] Bouslog, S.A., An, M.Y., Hartmann, L.N., and Derry, S.M. Review of Boundary Layer Transition Flight Data on the Space Shuttle Orbiter. Paper 91-0741, AIAA, January 1991.

[13] Goodrich, W.D., Derry, S.M., and Bertin, J.J. Shuttle Orbiter Boundary Layer Transition at Flight and Wind Tunnel Conditions. *Shuttle Performance: Lessons Learned*, NASA CP-2283 Part I, pg. 753-779, 1983.

[14] Harthun, M.H., Blumer, C.M., and Miller, B.A. Orbiter Windward Surface Entry Heating: Post-Orbital Flight Test Program Update. *Shuttle Performance: Lessons Learned*, NASA CP-2283 Part I, pg. 781-804, 1983.

[15] An, M.Y., Wang, K.C., Campbell, C.H., and Pelley, R.L. Space Shuttle Orbiter Aerodynamics Induced by Asymmetric Boundary-Layer Transition. Paper 96-0808, AIAA, January 1996.

[16] Schneider, S. P. and Skoch, C. Mean Flow and Noise Measurements in the Purdue Mach-6 Quiet-Flow Ludwieg Tube. Paper 2001-2778, AIAA, June 2001.

[17] Schneider, S.P., Matsumura, S., Rufer, S., Skoch, C., and Swanson, E. Hypersonic Stability and Transition Experiments on Blunt Cones and a Generic Scramjet Forebody. Paper 2003-1130, AIAA, January 2003.

[18] Schneider, S.P., Matsumura, S., Rufer, S., Skoch, C., and Swanson, E. Progress in the Operation of the Boeing/AFOSR Mach-6 Quiet Tunnel. Paper 2002-3033, AIAA, June 2002.

[19] Schneider, S.P., Rufer, S., Skoch, C., and Swanson, E. Hypersonic Transition Research in the Boeing/AFOSR Mach-6 Quiet Tunnel. Paper 2003-3450, AIAA, June 2003.

[20] Schneider, S. P., Skoch, C., Rufer, S., and Matsumura, S. Transition Research in the Boeing/AFOSR Mach-6 Quiet Tunnel. Paper 2002-0302, AIAA, January 2002.

[21] Ladoon, D. W. Wave Packets Generated by a Surface Glow Discharge on a Cone at Mach 4. PhD Thesis, School of Aeronautics and Astronautics, Purdue University, December 1998.

[22] Kwon, S. W. and Schneider, S. P. Stress Analysis for the Window of the Purdue Quiet-Flow

Ludwieg Tube. Paper 2002-309, AIAA, January 2002.

[23] Matsumura, S., Huang, C.-Y., Choi, Y.-S., Swanson, E. O., Salyer, T. R., and Sakaue, T. Feasibility of Detecting Streamwise Vortices from Roughness Elements Using Temperature Sensitive Paint in a Mach 4 Ludwieg Tube. Paper 2002-3238, AIAA, June 2002.

[24] Sakaue, H., Matsumura, S., Schneider, S. P., and Sullivan, J. P. Anodized Aluminum Pressure Sensitive Paint for Short Duration Testing. Paper 2002-2908, AIAA, June 2002.

[25] Matsumura, S., Berry, S.A., and Schneider, S.P. Streamwise-Vortex Instability and Transition on a Generic Scramjet Forebody. Paper 2003-3592, AIAA, June 2003.

[26] Schneider, S. P. Design of a Mach-6 Quiet-Flow Wind-Tunnel Nozzle Using the e**N Method for Transition Estimation. Paper 98-0547, AIAA, January 1998.

[27] Beckwith, I.E., Chen, F.-J., and Malik, M.R. Design and Fabrication Requirements for Low-Noise Supersonic/Hypersonic Wind Tunnels. Paper 88-0143, AIAA, January 1988.

[28] Schneider, S.P. Design and Fabrication of a 9.5-inch Mach-6 Quiet-Flow Ludwieg Tube. Paper 98-2511, AIAA, June 1998.

[29] Schneider, S.P. Fabrication and Testing of the Purdue Mach-6 Quiet-Flow Ludwieg Tube. Paper 2000-0295, AIAA, January 2000.

[30] Schneider, S.P., Rufer, S.J., Randall, L., and Skoch, C. Shakedown of the Purdue Mach-6 Quiet-Flow Ludwieb Tube. Paper 2001-0457, AIAA, January 2001.

[31] Schneider, S. P., Collicott, S. H., Schmisseur, J. D., Ladoon, D., Randall, L. A., Munro, S. E., and Salyer, T. R. Laminar-Turbulent Transition Research in the Purdue Mach-4 Quiet-Flow Ludwieg Tube. Paper 96-2191, AIAA, June 1996.

[32] Pate, S. Dominance of Radiated Aerodynamic Noise on Boundary-Layer Transition in Supersonic-Hypersonic Wind Tunnels. AEDC-TR-77-107, March 1978.

[33] Campbell, B.T., Liu, T., and Sullivan, J.P. Temperature Sensitive Fluorescent Paint Systems. Paper 94-2483, AIAA, June 1994.

[34] Liu, T., Campbell, B.T., Burns, S.P., and Sullivan, J.P. Temperature- and Pressure-Sensitive Luminescent Paints in Aerodynamics. *Applied Mechanics Review*, 50(4):227-246.

[35] Hamner, M.P. Demystifying Luminescent Paint Technology: A Guide for Non-Developers. Paper 2001-2981, AIAA, June 2001.

[36] Liu, T., Campbell, B.T., and Sullivan, J.P. Fluorescent Paint for Measurement of Heat Transfer in Shock-Turbulent Boundary Layer Interaction. *Experimental Thermal and Fluid Science*, 10:101-112, 1993.

[37] Liu, T., Campbell, B. T., Sullivan, J. P., Lafferty, J., and Yanta, W. Heat Transfer Measurement on a Waverider at Mach 10 Using Fluorescent Paint. *AIAA Journal of Thermophysics and Heat Transfer*, 9(4):605-611, October-December 1995.

[38] Hubner, J.P., Carroll, B.F., Schanze, K.S., Ji, H.F., and Holden, M.S. Temperature- and Pressure-Sensitive Paint Measurments in Short-Duration Hypersonic Flow. *AIAA Journal*, 39(4):654-659, April 2001.

[39] Nakakita, K., Osafune, T., and Asai, K. Global Heat Transfer Measurement in a Hypersonic Shock Tunnel Using Temperature-Sensitive Paint. Paper 2003-0743, AIAA, January 2003.

[40] Asai, K., Kanda, H., Kunimasu, T., Liu, T., and Sullivan, J.P. Boundary-Layer Transition Detection in a Cryogenic Wind Tunnel Using Luminescent Paint. *Journal of Aircraft*, 34(1):34-42, January-February 1997.

[41] Hamner, M.P., Popernack Jr., T.G., Owens, L.R., and Wahls, R.A. Using Temperature Sensitive Paint Technology. Paper 2002-0742, AIAA, January 2002.

[42] McLachlan, B.G., Bell, J.H., Gallery, J., Gouterman, M., and Callis, J. Boundary Layer Transition Detection by Luminescence Imaging. Paper 93-0177, AIAA, January 1993.

[43] Sakaue, H., Sullivan, J.P., Asai, K., Iijima, Y., and Kunimasu, T. Anodized Aluminum Pressure Sensitive Paint in a Cryogenic Wind Tunnel. Proceedings of the Instrumentation Society of America, 1999.

[44] Sakaue, H. and Sullivan, J.P. Fast Response Time Characteristics of Anodized Aluminum Pressure Sensitive Paint. Paper 2000-0506, AIAA, January 2000.

[45] Hubner, J.P., Carroll, B.F., and Schanze, K.S. Heat Transfer Measurements in Hypersonic Flow Using Luminescent Coating Techniques. Paper 2002-0741, AIAA, January 2002.

[46] Allison, S.W. and Gillies, G.T. Remote Thermography with Thermographic Phosphors: Instrumentation and Applications. *Review of Scientific Instruments*, 68(7):2615-2650, July 1997.

[47] Baker, W.M. Recent Experiences with Pressure Sensitive Paint Testing. Paper 2001-0135, AIAA, January 2001.

[48] Bell, J.H., Schairer, E.T., Hand, L.A., and Mehta, R.D. Surface Pressure Measurements Using Luminescent Coatings. *Annual Review of Fluid Mechanics,* 33:155-206, 2001.

[49] Creswell, L.A. and Cripps, M.N. Independent Pressure and Temperature Measurements from Double Layer Using Fluorescent Lifetime and Radiometric Imaging. Proceedings from the 8th PSP Workshop, Hampton, VA, October 2000.

[50] Iijima, Y., Kanda, H., Kunimasu, T., and Asai, K. Sample Tests of Temperature-Sensitive Paints with 18 Different Formulations (Japanese Text). 59th Wind Tunnel Research Conference, November 1997.

[51] Crafton, J., Lachendro, N., Guille, M., Sullivan, J.P., and Jordan, J.D. Application of Temperature and Pressure Sensitive Paint to an Obliquely Impinging Jet. Paper 99-0387, AIAA, January 1999.

[52] Chen, L.A. DuPont Titanium Technologies Technical Support. Private Communication, January 21, 2003.

[53] Cattafesta III, L.N. and Moore, J.G. Uncertainty Estimates for Luminescent Temperature-Sensitive Paint Intensity Measurements. Paper 95-2193, AIAA, June 1995.

[54] Novak, K. Rectification of Digital Imagery. *Photogrammetric Engineering & Remote Sensing*, 58:339-344, 1992.

[55] Donovan, J.F., Morris, M.J., Pal, A., Benne, M.E., and Crites, R.C. Data Analysis Techniques for Pressure- and Temperature-Sensitive Paint. Paper 93-0176, AIAA, January 1993.

[56] Weaver, W.L., Jordan, J.D., Dale, G.A., and Navarra, K.R. Data Analysis Methods for the Development and Deployment of Pressure Sensitive Paints. Paper 99-0565, AIAA, January 1999.

[57] Shimbo, Y., Noguchi, M., and Makino, Y. Blowdown Tunnel Application of Pressure Sensitive Paint. Paper 99-3169, AIAA, June 1999.

[58] Devereux, B.J., Fuller, M., Carter, L., and Parsell, R.J. Geometric Correction of Airborne Scanner Imagery by Matching Delaunay Triangles. *International Journal of Remote Sensing*, 11(12):2237-2251, 1990.

[59] Shanmugasundaram, R. and Samareh-Abolhassani, J. Modified Scatter Data Interpolation Used to Correct Pressure Sensitive Paint Images. Paper 95-2041, AIAA, June 1995.

[60] Bell, J.H. and McLachlan, B.G. Image Registration for Pressure-Sensitive Paint Applications. *Experiments in Fluids*, 22:78-86, 1996.

[61] Le Sant, Y. and Merienne, M-C. An Image Resection Method Applied to Mapping Techniques. Proceedings from ICIASF, IEEE, July 1995.

[62] Abdel-Aziz, Y.I. and Karara, H.M. Direct Linear Transformation from Comparator Coordinates into Object Space Coordinates in Close-Range Photogrammetry. Proceedings from the Symposium on Close-range Photogrammetry, pg 1-18, 1971.

[63] Liu, T. Geometric, Kinematic and Radiometric Aspect of Image-Based Measurements. Paper 2002-3239, AIAA, June 2002.

[64] Goffe, W. L., Ferrier, G. D., and Rogers, J. Global Optimization of Statistical Functions with Simulated Annealing. *Journal of Econometrics*, Vol. 60, No. 1-2, pg. 65-99, January-February 1994.

[65] Crossley, W.A. Genetic Algorithm for Global Optimization. AAE 590G, School of Aeronautics and Astronautics, Purdue University, 2000.

[66] Hollis, B.R. User's Manual for the One-Dimensional Hypersonic Aero-Thermodynamic (IDHEAT) Data Reduction Code. NASA CR-4691, August 1995.

[67] Asai, K., Kunimasu, T., and Iijima, Y. Visualization of the Quiet Test Region in a Supersonic Wind Tunnel Using Luminescent Paint. Proceedings from the 17th ICIASF, IEEE, September-October 1997.

[68] Berry, S.A. Auslender, A.H., Dilley, A.D., and Calleja, J.F. Hypersonic Boundary-Layer Trip Development for Hyper-X. *Journal of Spacecraft and Rockets*, 38(6):853-864, November-December 2001.

[69] Fay, J.A. and Riddell, F.R. Theory of Stagnation Point Heat Transfer in Dissociated Air. *Journal of Aerospace Sciences*, 25(2):73-85, 121, 1958.

[70] Daryabeigi, K., Berry, S.A., Horvath, T.J., and Nowak, R.J. Finite Volume Numerical Methods for Aeroheating Rate Calculations From Infrared Thermographic Data. Paper 2003-3634, AIAA, June 2003.

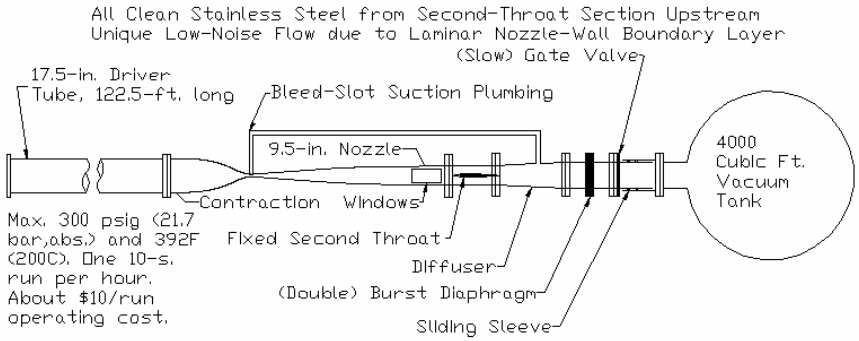

Figure 1. Schematic of the Boeing/AFOSR Mach-6 Quiet Tunnel.

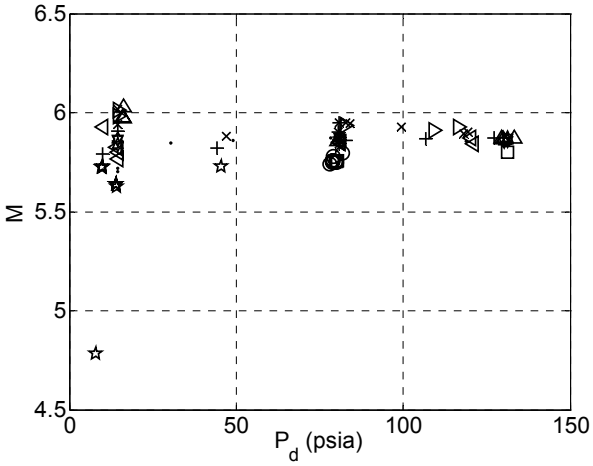

Figure 2. Freestream Mach number as a function of initial total pressure for several throat geometries, measured on the centerline 84.63±1/16 inches downstream of nozzle throat.

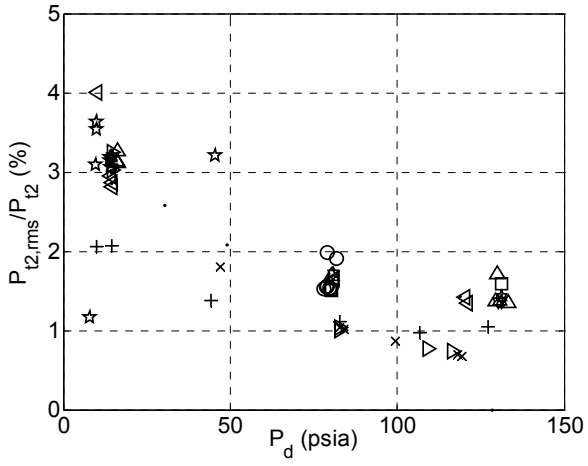

Figure 3. Freestream noise levels as a function of initial total pressure for several throat geometries, measured on the centerline 84.63±1/16 inches downstream of nozzle throat.

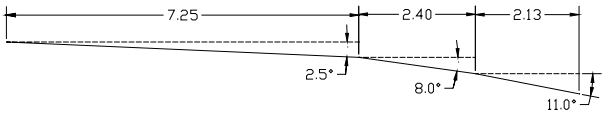

Figure 4. Sideview schematic of the centerline of the Hyper-2000 forebody.

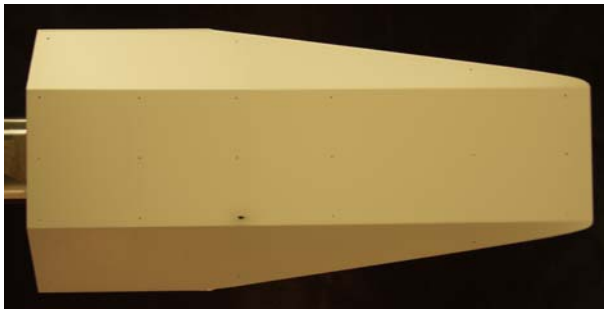

Figure 5. Picture of the Hyper-2000 forebody model.

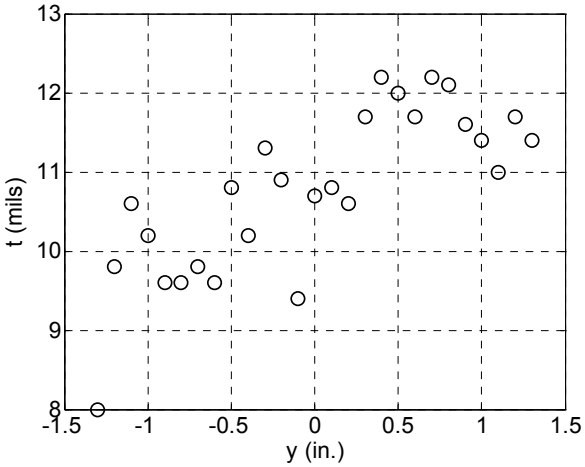

Figure 6. Leading edge thickness variation.

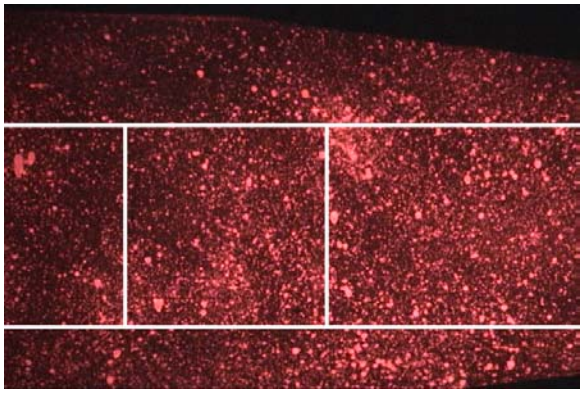

Figure 7. Image of the model with oil dots applied.

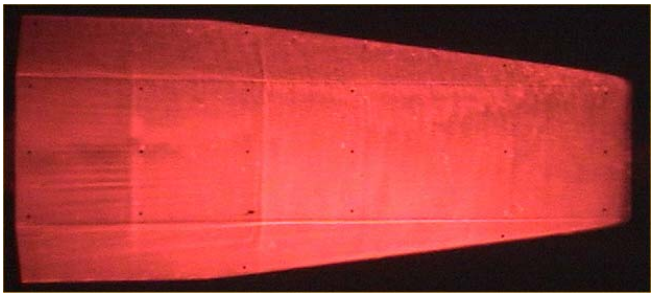

Figure 8A. Oil-flow raw video image with the painted approach immediately after tunnel startup.

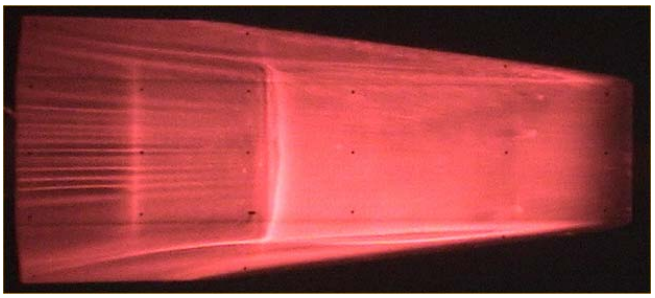

Figure 8B. Oil-flow raw video image with the painted approach 6.5 sec. into the tunnel run.

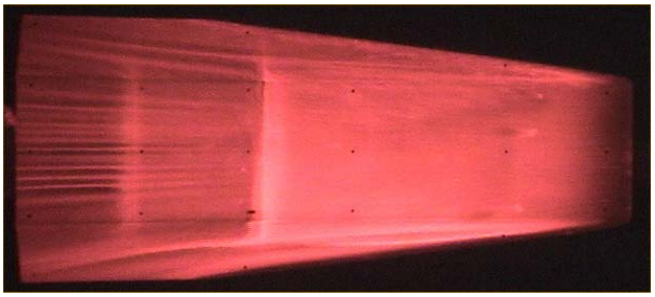

Figure 8C. Oil-flow raw video image with the painted approach immediately after tunnel unstart.

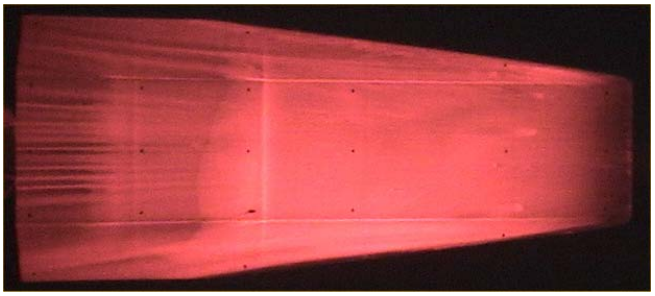

Figure 8D. Oil-flow raw video image with the painted approach 0.25 sec. after tunnel unstart.

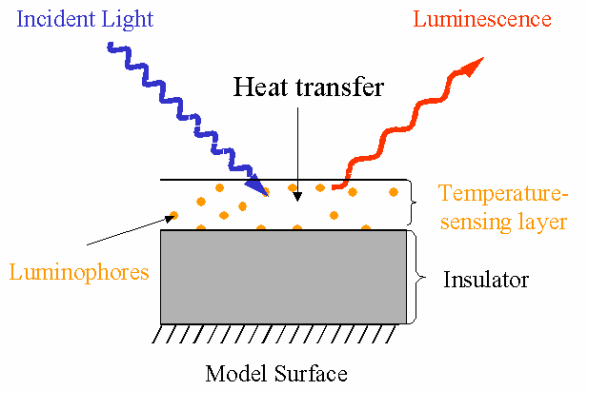

Figure 9. General schematic of a TSP layer over a model surface, adapted from Ref. [43].

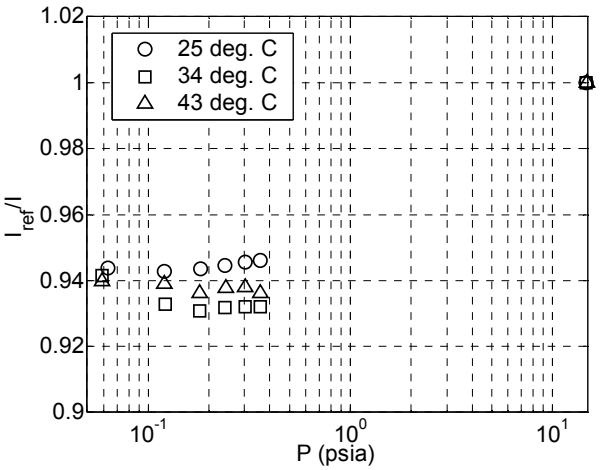

Figure 12. Sensitivity of the TSP at vacuum pressure at three temperatures.

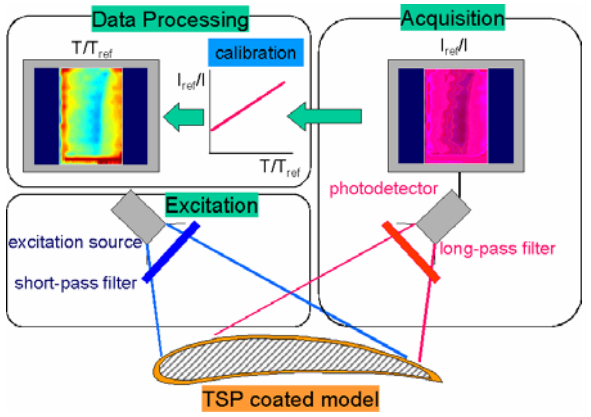

Figure 10. Schematic of the TSP experimental procedure, adapted from Ref. [44].

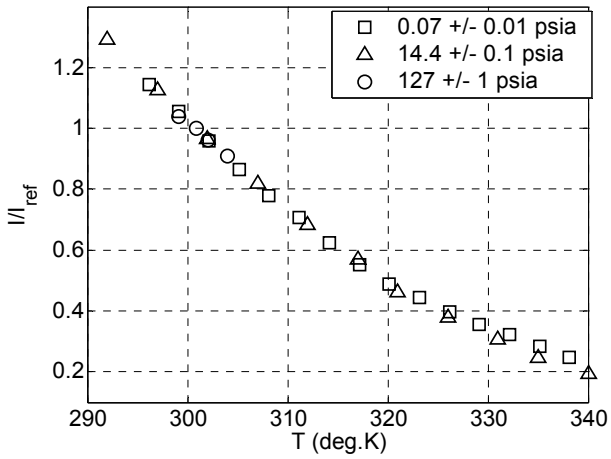

Figure 13. Comparison of temperature calibrations performed at vacuum, atmospheric, and high pressure conditions.

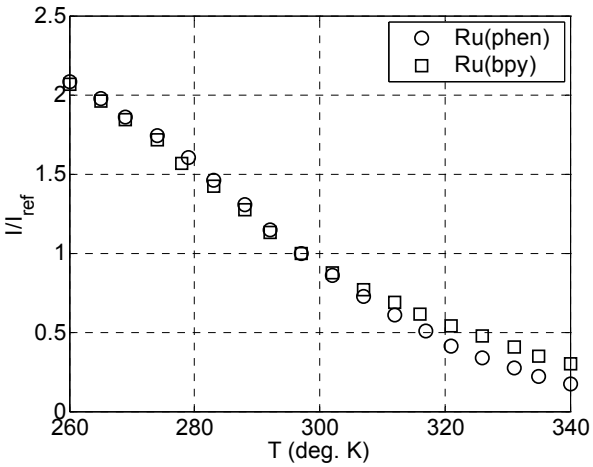

Figure 11. Comparison of the calibration data for Ru(bpy) and Ru(phen).

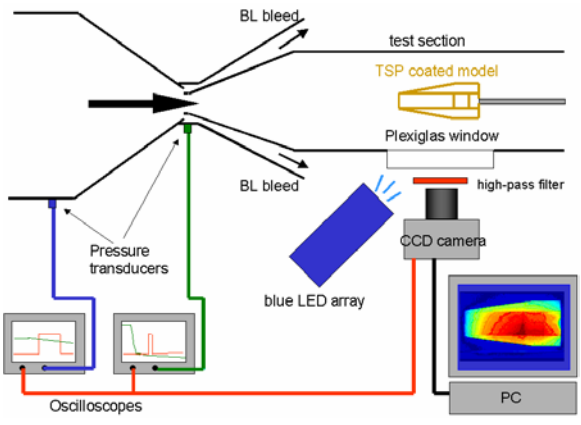

Figure 14. Schematic of the experimental setup.

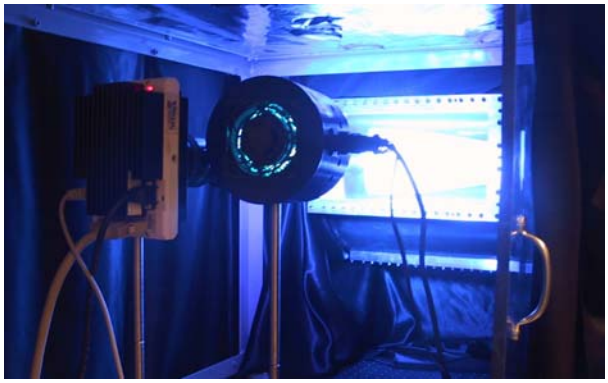

Figure 15. Image of the experiment setup.

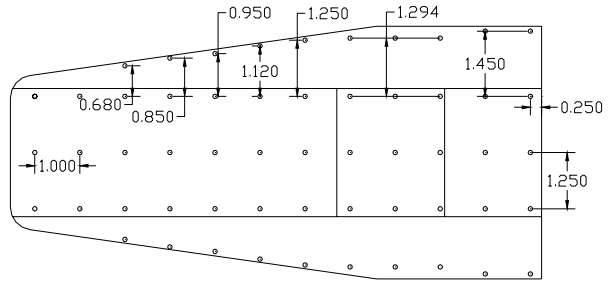

Figure 16. Locations of the registration marks used in the validation and optimization of the image processing method. All dimensions are in inches.

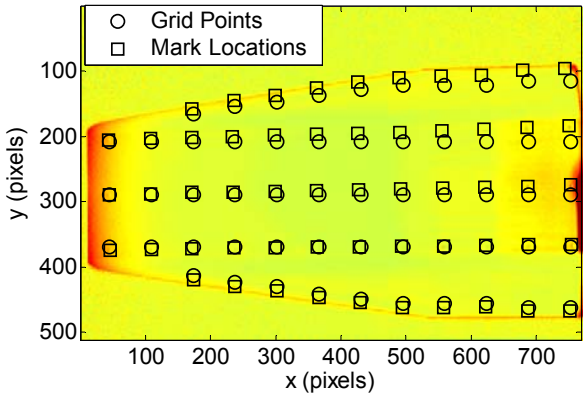

Figure 17. Intensity ratio of the wind-off and wind-on image, with the locations of the registration marks and their corresponding locations in the grid.

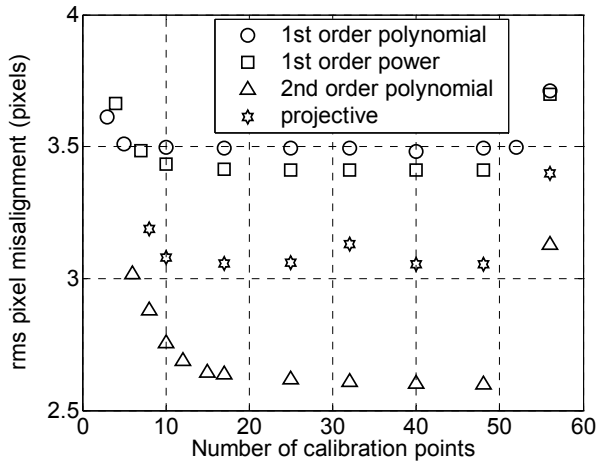

Figure 18. RMS pixel misalignment after applying the image registration equations for the optimized mark locations.

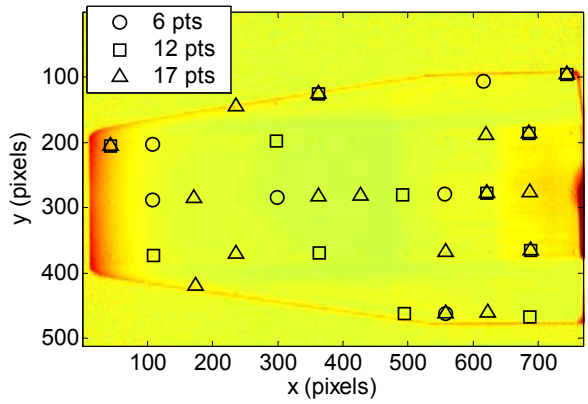

Figure 19. Optimized registration mark locations for the 2nd order polynomial image registration equation.

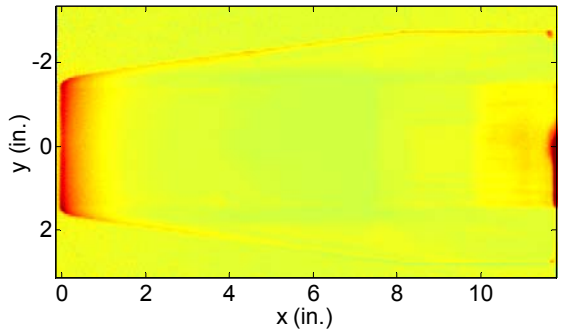

Figure 20. Intensity ratio image corrected using the 2nd order polynomial with 41 registration marks for calibration.

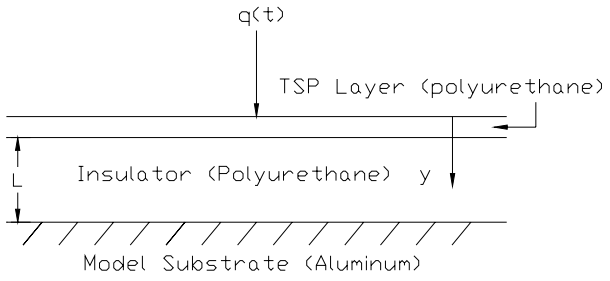

Figure 21. Thermal model of the heat transfer rate.

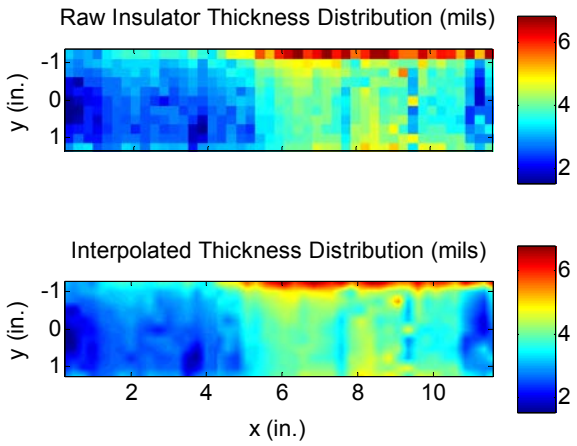

Figure 22. Insulator thickness distribution.

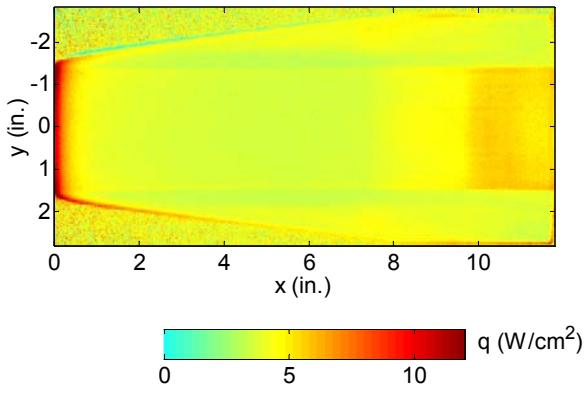

Figure 23. Heat-transfer rate image using the mean insulator thickness over the entire model.

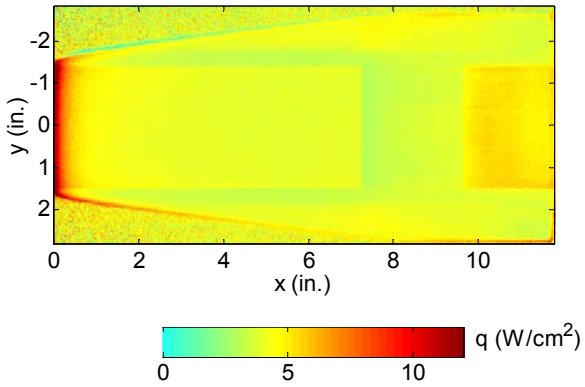

Figure 24. Heat-transfer rate image using the respective mean insulator thickness values on the three compression ramps and the chines.

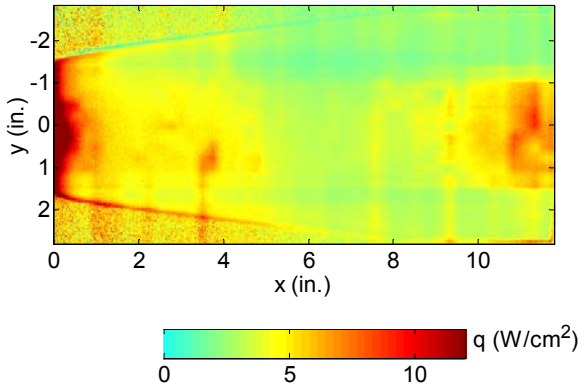

Figure 25. Heat-transfer rate image using an insulator thickness grid.

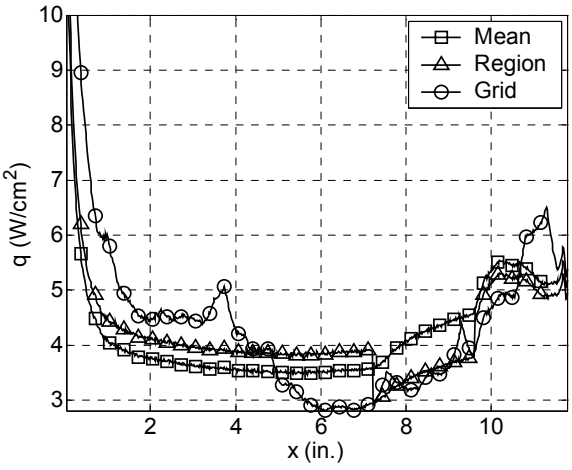

Figure 26. Streamwise mean heating distributions from three different treatment of the insulator thickness.

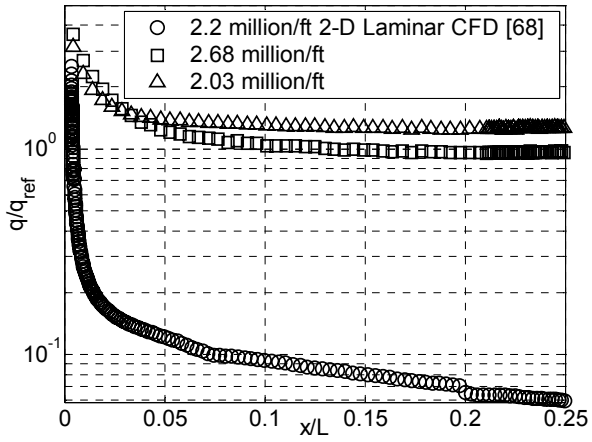

Figure 27. Comparison of heat-transfer rates to CFD data.

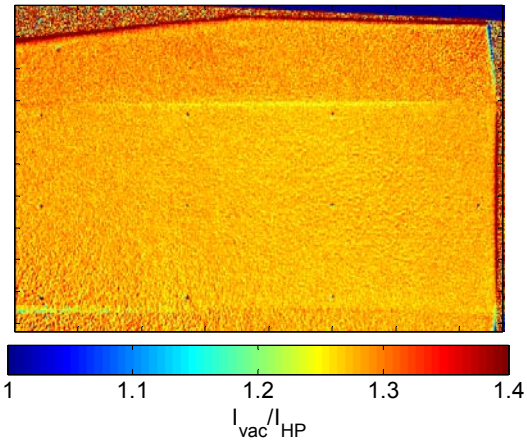

Figure 28. Ratio of TSP images taken at no-flow condition, with a temperature of 28.4 deg. C and pressures at 0.05 and 127 psia.

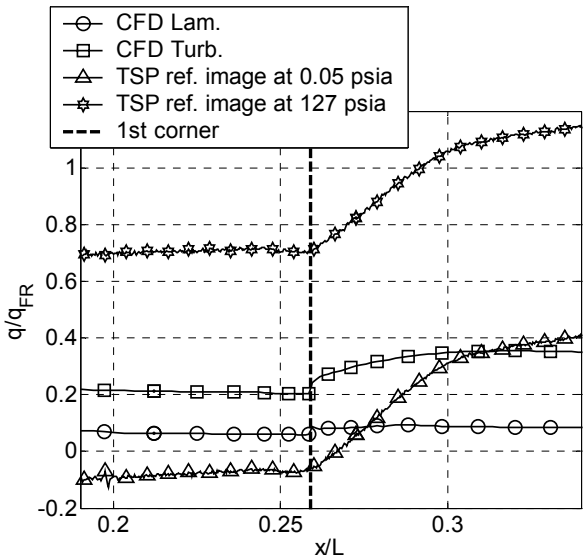

Figure 29. Comparison of the resulting heat-transfer rates using a wind-off image taken at 0.05 and 127 psia to CFD.

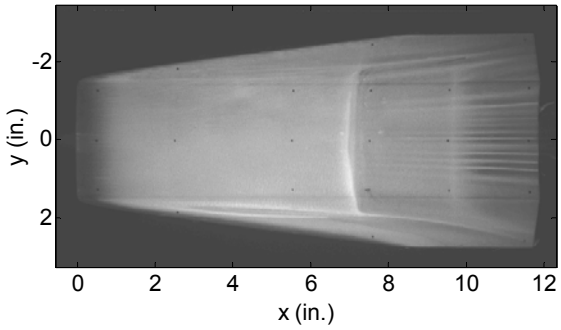

Figure 30. Oil-flow image with the painted-oil approach.

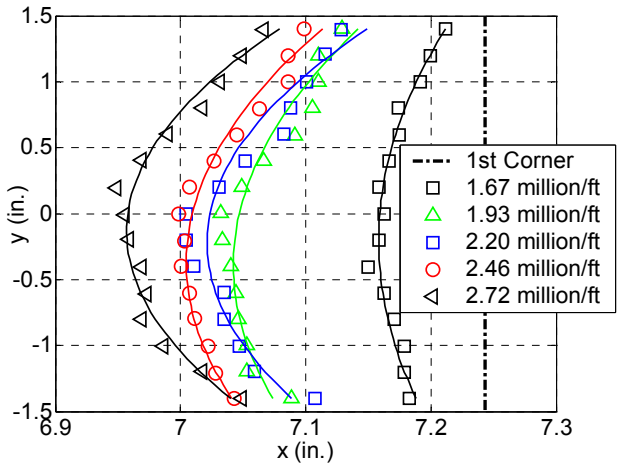

Figure 31. Unit Reynolds number effect on the separation line.

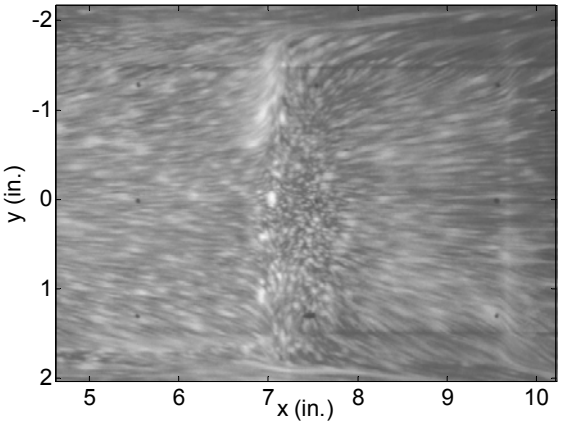

Figure 32. Oil-flow image with the oil-dot approach.

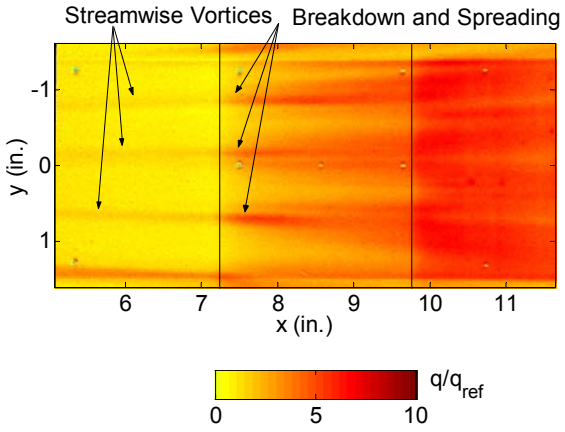

Figure 33. Normalized heat-transfer rate image.

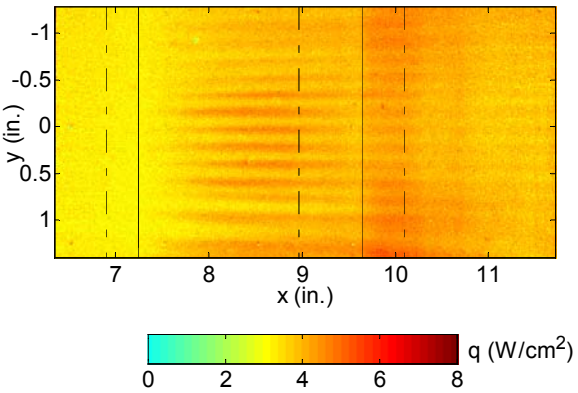

Figure 34. Heat-transfer rate image with 2.25 mil thick roughness spaced 0.16 inches apart, at total pressure of 129.5 psia (2.72 million/ft.).

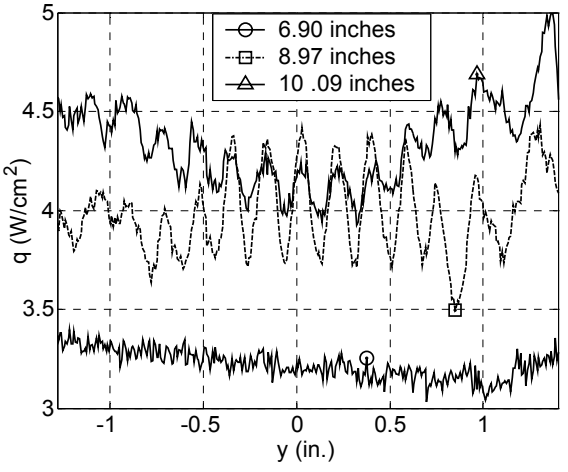

Figure 35. Spanwise heat-transfer rate distributions with 2.25 mil thick roughness spaced 0.16 inches at unit Reynolds number of 2.72 million/ft.

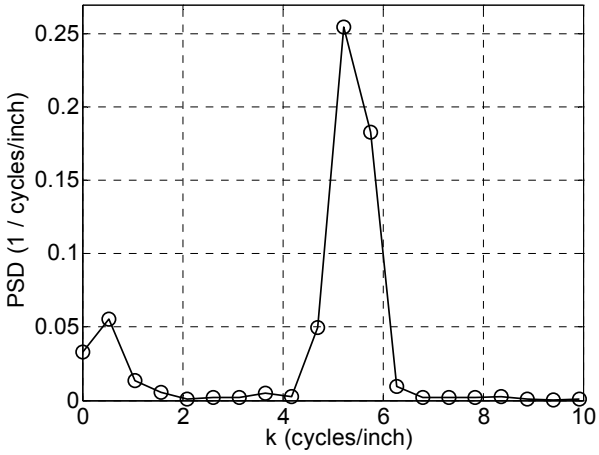

Figure 36. Power spectral density of the spanwise heat-transfer rate distribution at 8.97 inches from the leading edge with 2.25 mil thick roughness at 2.72 million/ft unit Reynolds number.

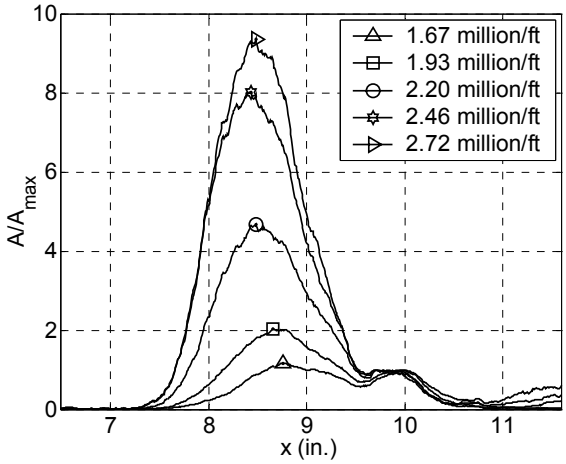

Figure 37. Streamwise distribution of the amplitude ratio for several unit Reynolds numbers using 2.25 mil thick roughness spaced 0.16 inches apart.